Materials Advances

ROYAL SOCIETY OF CHEMISTRY

PAPER

View Article Online
View Journal | View Issue

Cite this: *Mater. Adv.*, 2022, 3, 5451

Mixing of acoustic and optical excitations in Ru/Co based multilayers

P. Ntetsika,[a] G. Mitrikas,[b] G. Litsardakis[c] and I. Panagiotopoulos *[ad]

Two series of $[Ru_{10}/Co_x)]_{12}$ and $[Ru_6/Cr_3/Co_x)]_{12}$ x = 16–60 easy-plane anisotropy multilayers (all thicknesses in Å), prepared by sputter deposition, are studied by cavity FMR. The resonance fields of the modes excited by setting the rf field perpendicular to the saturating (in-plane) field are in good agreement with the values predicted for pure acoustic modes by a simple two-macrospin model. In contrast, the resonance fields of the modes excited by setting the rf field parallel to the saturating field, are lower than those expected for pure optical modes. This is attributed to the existence of hybridized mixed modes. Micromagnetic simulations show that (a) the inhomogeneous magnetization profile along the multilayer thickness is sufficient to give rise to mode mixing and (b) that mode mixing is not limited to the region where the frequencies of the acoustic and optical modes coincide.

Received 3rd February 2022,
Accepted 26th May 2022

DOI: 10.1039/d2ma00119e

rsc.li/materials-advances

Introduction

Synthetic antiferromagnets (SAFs) are based on the oscillatory interlayer exchange coupling of thin magnetic layers through metal, typically mediated by the Ruderman–Kittel–Kasuya–Yosida (RKKY) mechanism *via* the conduction electrons.[1] The low field tunability of the magnetic state in SAFs opened the route to the discovery of giant magnetoresistance phenomena and their implementation in spin-valves and magnetic tunnel junctions.[2] It is the same tunability that makes them attractive for other applications such as tunable magnonics[3–5] and terahertz nano-oscillators.[6–8] In early studies, the focus was on the optimization of the SAFs for spin valves while the study of dynamic properties was used mainly to derive anisotropies and interfacial coupling strengths.[9] Today there is a renewed interest in SAF systems for their dynamic properties and for their possible incorporation in synthetic antiferromagnetic spintronic structures.[10]

The antiferromagnetic interlayer exchange coupling in SAFs gives rise to two distinct modes (acoustic/optical) distinguished according to the correlation of the magnetic moment precession between adjacent magnetic layers. As the names indicate, for acoustic modes the resonances approach zero at zero field, while the optical modes possess useful high frequencies at zero-applied field.[11] Several works have focused on these aspects of SAF systems in FeCoB/Cr/FeCoB,[12] FeCoB/Al_2O_3/FeCoB,[13] Pt/Co/Ir/Co/Pt,[14] and CoFeB/Ru/CoFeB.[15,16] A study based on an all-optical pump-probe technique showed that the dynamic exchange coupling increased the damping of the optical mode owing to the spin-pumping effect at the CoFeB/Ru interfaces.[17] The frequencies of the modes, as a function of the applied field, depend on the magnetic state and therefore on the uniaxial magnetic anisotropy (H_K) and antiferromagnetic interlayer exchange coupling (H_{ex}), which provide control of the dynamic properties. Thus, the frequencies of the modes can be used to extract the coupling and anisotropy parameters as has been used in early[18] and recent studies.[6] As the frequencies of the optical and acoustic modes depend on the applied field, there is a point where they tend to coincide. It has been shown that the optical and acoustic spin-wave modes get hybridized at these degeneracy points.[4,5,19] The mode coupling is reported to be mediated by the dipolar fields generated by the magnetization motion of spin waves and the out-of-plane tilt angle.[4] It therefore increases with the wave number of excited spin waves and the angle between the external magnetic field and spin-wave propagation directions[5] and can be enhanced by applying an out of-plane bias field[20] or constructing a structurally asymmetrical SAF.[19] Here, we expand these studies to multilayer systems, where other mode mixing mechanisms may come into play. We present a Ferromagnetic Resonance (FMR) study of two series of $[Ru_{10}/Co_x)]_{12}$ and $[Ru_6/Cr_3/Co_x)]_{12}$ x = 16–60 multilayers (all indices inside the brackets denote thickness in Å, the index 12 refers to the repetitions of the period of the stack). The films have been prepared by sputter deposition and have easy-plane anisotropy but no anisotropy within the plane. The use of chromium gives an extra degree of

[a] *Department of Materials Science and Engineering, University of Ioannina, Ioannina 45110, Greece. E-mail: ipanagio@uoi.gr*
[b] *Institute of Nanoscience and Nanotechnology, National Centre for Scientific Research-Demokritos, Athens, Greece*
[c] *Laboratory of Materials for Electrotechnics, Department of Electrical and Computer Engineering, Aristotle University of Thessaloniki, Thessaloniki, Greece*
[d] *Institute of Materials Science and Computing, University Research Center of Ioannina (URCI), 45110 Ioannina, Greece*

freedom in tailoring the exchange coupling and anisotropy independently as both have interfacial contributions that scale inversely with the layer thickness. Co/Cr heterostructures have received much less attention than Fe/Cr since there is a crystal structure mismatch between Cr and Co.[21] It is found that the $[Ru_{10}/Co_x)]_{12}$ can give higher zero-field optical modes and therefore has more interesting dynamical properties. We propose that mode coupling is linked to the inhomogeneous magnetization profile along the multilayer thickness. Thus, the mode mixing is not limited to the region where the frequencies of the optical and acoustic modes coincide.

Experimental details

The multilayered $[Ru_{10}/Co_x)]_{12}$ and $[Ru_6/Cr_3/Co_x)]_{12}$ (with x = 14–60, all thicknesses in Å) films have been deposited on rotating substrates, at room temperature by magnetron sputtering, using a multi-source deposition system. The values of the Ru and Ru/Cr layer thickness were chosen to maximize the RKKY exchange interactions in each case. The Co, Cr (7.62 cm diameter) and Ru (5.08 cm diameter) sources are in confocal geometry: *i.e.*, pointing at an angle of 45 deg to the (horizontal) substrate plane, which is rotated during the deposition. The target to substrate distance is 15 cm. Prior to the deposition, the chamber was evacuated to a base pressure better than 7×10^{-5} Pa and the process gas (Ar) pressure during deposition was 0.47 Pa. Co has been deposited at a rate of 0.75 Å s^{-1} by applying a DC power of 100 W, chromium at 1.15 Å s^{-1} with 130 W DC, and Ru at 0.40 Å s^{-1} using 120 W RF. The samples were sputtered on thermally oxidized Si(100) wafers. The magnetic measurements were done using a vibrating sample magnetometer (VSM) of Lakeshore Cryotronics Inc. (model 7312) with eight sensing coils (four per component) and a 20 kOe electromagnet and a QD Versalab VSM with 30 kOe field. The ferromagnetic resonance (FMR) measurements were performed at room temperature using a Bruker ESP 380E spectrometer equipped with a rectangular ER 4102ST or a dual-mode ER 4116DM cavity. The dc-field was always in the film plane. When the exciting rf field is parallel to the dc-field the excitation of optical modes for which the motion of the spins is symmetric with respect to the dc-field direction are favored. On the other hand, setting the rf field perpendicular to the dc favors the excitation of acoustic modes. The microwave frequency was measured with a HP 5350B microwave frequency counter. Spectra were obtained using a microwave power of 20.9 mW, modulation frequency of 100 kHz, modulation amplitude of 1 mT, a field-sweep range of 450 mT and an acquisition time of 167 s. The cavity frequencies were 9.76 GHz for the rf($\perp$) and 9.34 for the rf($\parallel$) measurements.

Magnetic properties and FMR

Since the films are deposited on rotating substrates there is no anisotropy within the film plane. VSM measurements have been used to characterize the anisotropy and the coupling strength between the layers. The shape anisotropy is the dominant term: for all the films the saturation field within the plane $H_\parallel$ is lower than the saturation field along the film normal $H_\perp$. In short, the anisotropy is easy plane, but without any preferential orientation within the film plane. Due to the lack of anisotropy within the plane, the scissor-like magnetization state between successive Co layers (due to the competition between the interlayer AF coupling and dc magnetic field) is attained gradually, without any spin-flop transition.[22] The RKKY exchange field n be estimated from the in-the plane saturation field $H_\parallel = \dfrac{4J_{AF}}{M_s t_{Co}} = 2H_{ex}$. The factor 2 enters because each Co layer is coupled to two neighbouring layers. This holds strictly only for an infinite layer stack, without outer layers. However, for our case with N = 12 Co layers, the micromagnetic simulations (Section 4) show that the effect of the two outer layers (which are coupled to only one layer) is negligible. For the measurements along the film normal apart from the shape anisotropy, the magnetocrystalline (K_{mc}) and interfacial anisotropy (K_S) contributions must also be considered. The total uniaxial anisotropy would be $K_{eff} = -\dfrac{1}{2}\mu_0 M_s^2 + K_{mc} + \dfrac{2K_S}{t_{Co}}$ and the field H_K required for perpendicular saturation in opposition to the anisotropy is $\mu_0 H_K = \mu_0 M_s - \dfrac{2K_{mc}}{M_S} - \dfrac{4K_S}{M_S t_{Co}} < \mu_0 M_S$. The values of H_{ex} and H_K are estimated by the saturation field parallel and perpendicular to the film plane $H_\parallel$, $H_\perp$ respectively using $H_\parallel = 2H_{ex}$, $H_\perp = H_K + 2H_{ex}$. Typical curves for $[Ru_{10}/Co_{30})]_{12}$ and $[Ru_6/Cr_3/Co_{30})]_{12}$ samples are shown in Fig. 1. The obtained values are summarized in Table 1 along with the FMR resonance fields. The dependence of H_{ex} and H_K on the Co layer thickness is presented in Fig. 2. The thickness dependences can be explained by the decreasing interfacial contributions as the thickness increases: the main contribution to H_K is the shape anisotropy. Thus, the total anisotropy is in-plane. The interfacial contribution tends to drive the anisotropy to the perpendicular and reduces the absolute value of H_K. Therefore, H_K increases with Co thickness. On the other hand, for in-plane measurements, the exchange field is mainly of interfacial origin, so it is expected to decrease with thickness. Some deviations may arise from magnetostatic coupling.

For fields lower than $2H_{ex}$, the sample is unsaturated and the acoustic and optical resonances are expected at:[4]

$$\begin{aligned} f_{ac} &= \gamma\mu_0 H\sqrt{1+\frac{H_K}{2H_{ex}}}, \\ f_{opt} &= \gamma\mu_0\sqrt{2H_{ex}H_K}\sqrt{1-\left(\frac{H}{2H_{ex}}\right)^2} \end{aligned} \quad (1)$$

where H_K is the effective anisotropy field which includes all magnetocrystalline, interfacial and shape anisotropy contributions. These equations imply that there is a field value $H^* = \sqrt{2}H_{ex}/\sqrt{1+H_{ex}/H_K}$ for which the frequencies of the optical and acoustic branches coincide. For fields $H_\parallel > 2H_{ex}$ the sample is saturated, and the acoustic resonance coincides

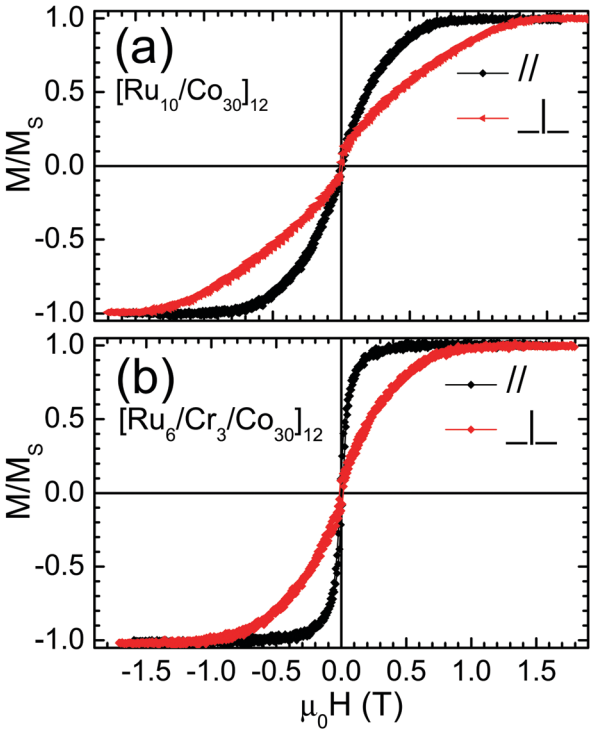

Fig. 1 Typical VSM magnetization curves for (a) $[Ru_{10}/Co_{30}]_{12}$ and (b) $[Ru_6/Cr_3/Co_{30}]_{12}$ samples. These curves are full loops from positive saturation to negative and back to positive. The paths of the two branches coincide.

with that of a single ferromagnetic layer

$$f_{ac} = \gamma\mu_0\sqrt{H(H+H_K)} \tag{2}$$

whereas the optical resonance is suppressed.

The FMR spectra are presented in Fig. 3. Using the $H_\parallel$, $H_\perp$ obtained from the VSM data we derive the parameters H_{ex} and H_K. Then using eqn (1) (with the frequencies set to the cavity frequency f_c), the expected field values of the acoustic and optical FMR resonances (H_{ac}, H_{opt}) can be calculated as:

$$H_{ac} = \frac{f_c}{\gamma\mu_0\sqrt{1+\dfrac{H_K}{2H_{ex}}}} \tag{3a}$$

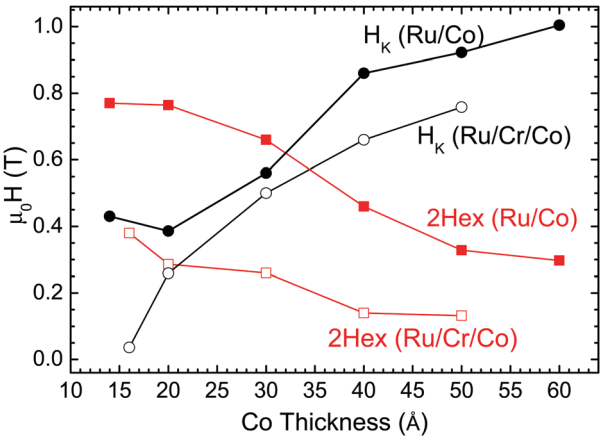

Fig. 2 Dependence of interlayer exchange field H_{ex} (squares) and anisotropy field H_K (circles) on Co layer thickness for $[Ru_{10}/Co_{30}]_{12}$ (solid symbols) and (b) $[Ru_6/Cr_3/Co_{30}]_{12}$ series (open symbols).

$$H_{opt} = 2H_{ex}\sqrt{1-\left(\frac{f_c}{\gamma\mu_0\sqrt{2H_{ex}H_K}}\right)^2} \tag{3b}$$

The application of an rf field perpendicular/parallel to the in-plane dc field favours the excitation of acoustic/optical modes respectively.[4,23] Thus the H_{ac} and H_{opt} should be compared to the experimentally observed FMR resonance fields $H_{res}(\perp)$ and $H_{res}(\parallel)$ obtained when rf$\perp$dc and rf$\parallel$dc respectively. For the acoustic resonances there is a fair agreement between the calculated values and those observed by FMR for $\gamma = 32$ GHz/T, a value which is close to that obtained for Pt/Co/W multilayers prepared under the same conditions.[24] The $[Ru(10)/Co(14)]_{12}$ sample did not give a measurable signal in the FMR. The expected frequency of the zero-field optical mode $f_o(0) = \gamma\mu_0\sqrt{2H_{ex}H_K}$, which is interesting for applications, is between 17.4 and 20.1 GHz for the $[Ru_{10}/Co_x]_{12}$ series. For the $[Ru_6/Cr_3/Co_x]_{12}$ series it takes lower values, ranging between 4 and 11.5 GHz. The FMR measurements with rf$\parallel$dc did not give resonances for any of the $[Ru(6)/Cr(3)/Co(x)]_{12}$ samples. This can be partially attributed to the fact that for most of these

Table 1 Saturation fields derived from VSM data, resonance fields for acoustic and optical modes calculated by a macrospin model based on the VSM data, and experimentally observed peaks $\mu_0 H_{res}$ by FMR with different orientations of the rf field. All values are in Tesla

	VSM		Macrospin model		FMR (rf$\perp$dc and rf$\parallel$dc)	
Layering	$\mu_0 H_\parallel$	$\mu_0 H_\perp$	$\mu_0 H_{ac}$	$\mu_0 H_{opt}$	$\mu_0 H_{res}$ ($\perp$)	$\mu_0 H_{res}$ ($\parallel$)
$[Ru(10)/Co(14)]_{12}$	0.77	1.20	0.24	0.66	—	—
$[Ru(10)/Co(20)]_{12}$	0.76	1.15	0.25	0.64	0.25	—
$[Ru(10)/Co(30)]_{12}$	0.66	1.22	0.22	0.58	0.22	0.39
$[Ru(10)/Co(40)]_{12}$	0.46	1.32	0.18	0.41	0.19, 0.12	0.34, 0.21, 0.09, 0.03
$[Ru(10)/Co(50)]_{12}$	0.33	1.25	0.16	0.28	0.14	0.12
$[Ru(10)/Co(60)]_{12}$	0.30	1.30	0.15	0.25	0.12	0.07
$[Ru(6)/Cr(3)/Co(16)]_{12}$	0.38	0.42	0.24	—	0.25	—
$[Ru(6)/Cr(3)/Co(20)]_{12}$	0.29	0.55	0.29	—	0.21	—
$[Ru(6)/Cr(3)/Co(30)]_{12}$	0.26	0.76	0.18	0.14	0.16	—
$[Ru(6)/Cr(3)/Co(40)]_{12}$	0.14	0.80	0.13	—	0.15	—
$[Ru(6)/Cr(3)/Co(50)]_{12}$	0.13	0.89	0.12	0.34	0.12	—

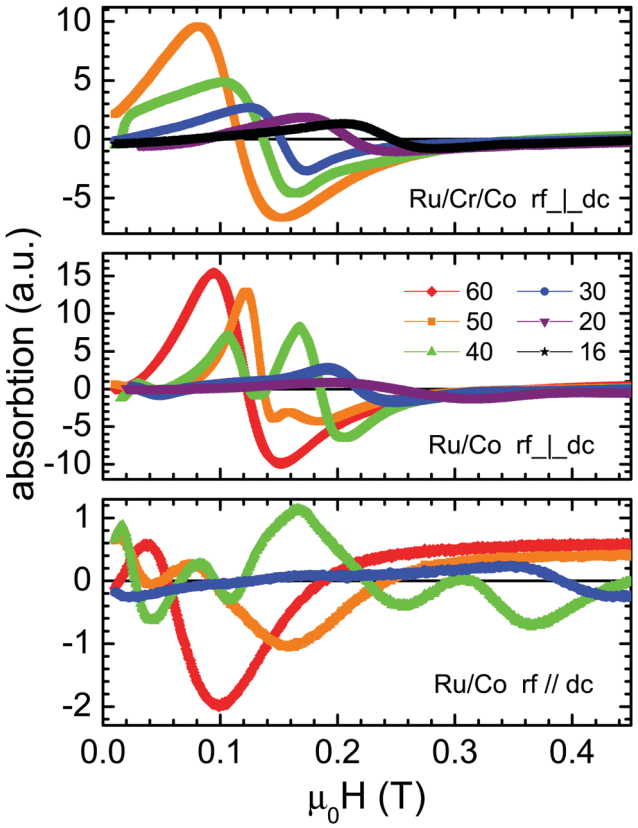

Fig. 3 FMR spectra for different multilayers measured with the rf perpendicular/parallel to in-plane dc field. The numbers indicate the Cobalt layer thickness in Å.

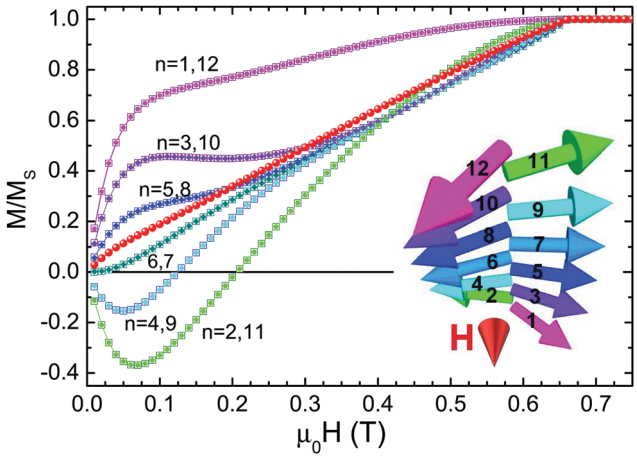

Fig. 4 Simulated magnetization curve (red circles) of a SAF consisting of 12 Co layers compared to the magnetization of each of the twelve layers. The layer numbers are written next to each of the curves. While the total magnetization is very close to the linear dependence predicted by a two-macrospin model, the individual layers show significant deviations. The outer layers (1,12) that are coupled only on one side, are the first to move towards the field forcing their neighboring layers (2,11) to the opposite direction due to the AF coupling. The inset shows the configuration for μ_0H = 0.23 T. Each of the vectors is a macrospin along the direction of the moment of the layer. Coloring is done according to the cosine with the direction of the applied field (small red cone).

samples $f_o(0)$ is below the rf frequency of the cavity and according to eqn (3b) cannot be observed:

The $[Ru(10)/Co(20)]_{12}$ samples gave resonances with rf‖dc but at frequencies which are lower than those of the expected pure optical modes. For $[Ru(10)/Co(40)]_{12}$ the higher resonance is at a value 0.34 T, between the calculated H_{ac}, H_{opt} whereas the second is very close to the H_{ac}. Similarly, the $[Ru(10)/Co(30)]_{12}$ sample resonance field value of 0.39 T lies between H_{ac} and H_{opt}. For rf‖dc resonances below H_{ac} appear. These findings can be qualitatively explained by hybridization of optical and acoustic modes, in accordance with the discussion of micromagnetic simulations' results in the next section.

Micromagnetic simulations

The micromagnetic simulations have been done using the mumax3 package[25] for a model system of 12 Co layers of thickness t_{Co} = 25 Å, with antiferromagnetic interlayer coupling. Based on the magnetic measurements the saturation magnetization was set to M_S = 1160 kA m^{-1} and the uniaxial anisotropy to K_{mc} = 460 kJ m^{-3} which represents a typical value for our samples. It is larger than the 290 kJ m^{-3} of the single Co layer due to the interfacial contributions. Note that these values are lower than the $\mu_0 M_S^2$ = 1690 kJ m^{-3} required for perpendicular anisotropy. Thus, the magnetization is easy-plane. The bulk intralayer exchange stiffness was set to A_{ex} = 17 pJ m^{-1}.[26] The interfacial RKKY exchange was set to $J_{AF} = -0.5$ mJ m^{-2} The cell size was set to 2.5 nm which is smaller than the characteristic exchange length scale $L_{ex} = \sqrt{2A_{ex}/\mu_0 M_S^2} = 4.5$ nm. The lateral simulation cell size was set to 320 nm × 320 nm. An array of 10 × 10 extra in-plane images was set, as pseudo-periodic boundary conditions, to better account for the demagnetizing field of thin film geometry.

In Fig. 4 the total magnetization as a function of the applied field is shown for the multilayer and is compared with the curves for each of the constituent Co layers. The total magnetization increases linearly and reaches saturation at a value of 0.67 Tesla. This is exactly what is predicted by a two-macrospin model for which the saturation field should be $\mu_0 H_\parallel = \mu_0 2H_{ex} = 4J_{AF}/(M_s t_{Co})$. The factor 2 accounts for the fact that each layer is coupled on both sides. The fact that the two outer layers are not coupled on both sides does not seem to affect the response of the multilayer as a whole: It does not even lead to a reduction of $(N-1)/N = 11/12$ (where N is the number of layers) as a simple linear scaling would suggest. To check this fact, we have also simulated N = 2,4 and 8. For N = 2 we get the expected value $\mu_0 H_\parallel = \mu_0 H_{ex} = 2J_{AF}/(M_s t_{Co})$. For N = 4 we get 87% instead of 75% of $2H_{ex}$, and for N = 8 we already get 98.5% instead of 87.5% of the $2H_{ex}$. However, the lack of coupling of the outer layers (n = 1, 12 at Fig. 4) has a significant impact on their saturation which proceeds much faster that the average linear dependence. This forces their adjacent layers (n = 2, 11) to the opposite direction and so on, yielding the layer dependent approach to saturation sketched in Fig. 4. In short, at a specific

applied external field the symmetry axis of the scissor state varies along the film thickness. Due to the symmetry the dependence of the n-th layer coincides with that of the (13-n)th.

The resonance frequencies are extracted following the methods and considerations described in ref. 27 for each magnetic state (different dc field value H) along the saturation curve, an exciting external field having a time dependence following a sinc function, is applied and the resulting magnetic response is Fourier analysed. The sampling time step was set to 5 ps (frequencies up to 100 GHz) and the exciting field amplitude was $\mu_0 H_{rf}$ = 1 mT. The peaks of the Fourier transform correspond to the resonance modes. Setting the sinc pulse perpendicular/parallel to the dc field H (always in-plane) favours the excitation of acoustic/optical modes respectively.[4] A 2D-contour map of the Fourier transform amplitude as a function of frequency and applied field is shown in Fig. 5. The plotted quantity is the amplitude of the variation of the magnetization component δM along the direction of H_{rf} divided by the H_{rf} amplitude $\chi = \left(\frac{1}{H_{rf}} \cdot \frac{\delta M}{M_s}\right)$. The frequency is normalized to the value $\gamma\mu_0\sqrt{2H_{ex}H_K}$ of the zero-field optical mode. The applied field is normalized to the saturation field against the AF exchange interlayer coupling which is equal to $2H_{ex}$. On the contour maps the frequencies predicted by eqn (1) and (2) are superimposed. The H^* is the field at the point where the acoustic (blue) and optical (red) curves meet. Fig. 5 shows that at even low applied fields several modes of mixed character with frequencies between those of the acoustic and optical branches are exited. All modes can be characterized by the phase difference of the precession between the consecutive cobalt layers. In an ideal acoustic mode, the phase difference should be zero while for an ideal optical mode, it is expected to be 180 deg. Plots giving the phase difference between consecutive cobalt layers are shown in Fig. 6.

The modes with frequencies close to those predicted by the macrospin model (blue and red lines in Fig. 5) have profiles closer to what is expected for pure modes of either acoustic or optic character. Mode "(a)" has phase differences $\delta\varphi$ close to 180 deg, except for the outer layers, for which $\delta\varphi$ = 125 deg. Therefore, it is close to what is expected for an optical mode. Mode "(i)" has phase differences $\delta\varphi$ close to zero, except for the outer layers for which $\delta\varphi$ = 8 deg. Thus, it is close to what is expected for an acoustic mode. The rest of the modes have mixed character. The existence of these mixed resonances can explain the extra FMR peaks observed in some samples as well

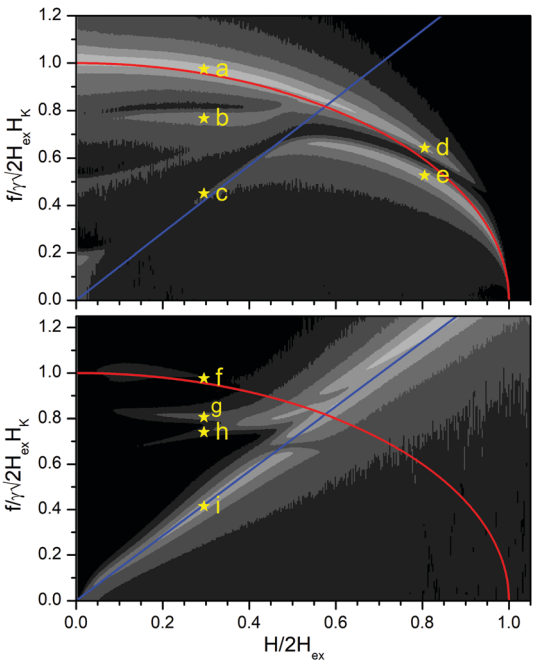

Fig. 5 Amplitude of FFT transform of the magnetization component along the exciting rf field as a function of frequency and dc field for a $[Ru/Co)]_{12}$ SAF multilayer. The plotted quantity is $\chi = \left(\frac{1}{H_{rf}} \cdot \frac{\delta M}{M_s}\right)$. The upper/lower panels are derived by setting the exciting rf field parallel/perpendicular to the magnetizing dc field respectively. The color map (between black and white) is not linear but corresponds to the values $0^3 \times 10^{-3}$, 0.6×10^{-3}, 1.2×10^{-3}, 2.4×10^{-3}, 4.8×10^{-3}, 9.6×10^{-3} and 19.2×10^{-3}. The frequencies predicted by the macrospin model (eqn (1) and (2)) are superimposed. A red curve is used for the optical mode and blue for the acoustic. The mode profiles at the points marked by the star symbols (a–i) are given in Fig. 6.

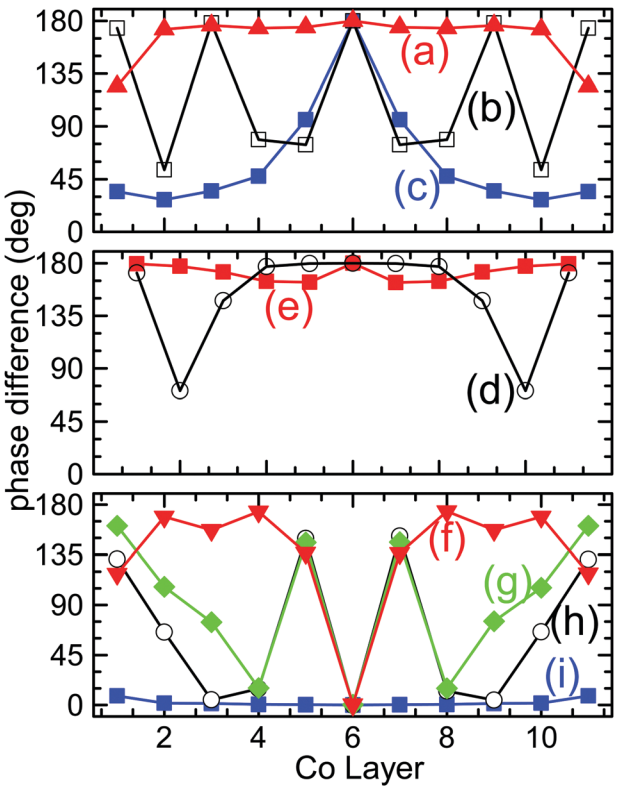

Fig. 6 Mode profiles: The phase difference of the precessional motion between consecutive cobalt layers for the points marked by the star symbols (a–i) in Fig. 5. The X-axis denotes the number n of the layer and the y axis the phase difference between the n-th and the (n + 1)-th layer. The profile (a) is closer to a pure optical mode whereas the profile (i) is closer to a pure acoustic mode. The rest of the profiles indicate a mixed character.

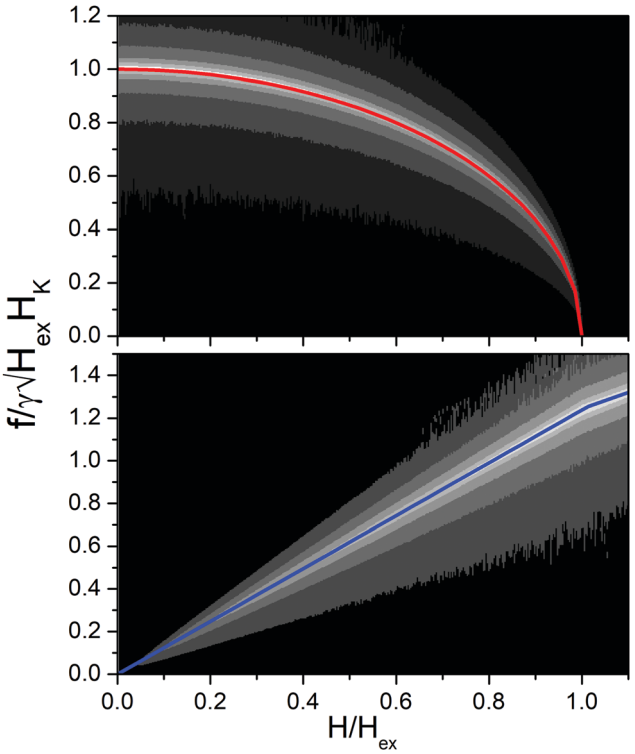

Fig. 7 Amplitude FFT transform of the magnetization component along the exiting rf field as a function of frequency and dc field for a [Ru/Co]$_2$ SAF bilayer. The plotted quantity is $\chi = \left(\frac{1}{H_{rf}} \cdot \frac{\delta M}{M_s}\right)$. The upper/lower panels are derived by setting the exciting rf field parallel/perpendicular to the magnetizing dc field respectively. The color map (between black and white) is not linear but corresponds to the values 1×10^{-3}, 2×10^{-3}, 4×10^{-3}, 8×10^{-3}, 12×10^{-3}, and 16×10^{-3}. The frequencies predicted by the macrospin model (eqn (1) and (2), but with $2H_{ex} \rightarrow H_{ex}$) are superimposed. A red curve is used for the optical mode and blue for the acoustic.

as the fact that their frequencies are lower than those expected by the simple macrospin model.

The micromagnetic simulation of Fig. 5 can serve as a basis to qualitatively understand the deviations of the optical modes from the expected values of the macrospin modes. For the $[Ru_{10}/Co_x]_{12}$ samples the values of $f_{cavity}/\left(\gamma\sqrt{2H_{ex}H_K}\right)$ range between 0.48 to 0.56. In this region, there is a strong deviation between the predictions of the macrospin model and the exact micromagnetic model which gives a splitting of the optical mode. For a specific frequency (*i.e.* a specific horizontal line in Fig. 5) there will be two resonance fields: one below and one above the one predicted by the macrospin model (red curve). Of course, as each sample has its own parameters H_{ex}, H_K a different simulation should be done in each case using the sample specific parameters. For the $[Ru_{10}/Co_{40})]_{12}$ sample for instance the FMR rf$\|$dc the macrospin model predicts a peak at 0.41 Tesla, but the optical mode at 0.41 is split into two modes (0.35 Tesla and 0.43 Tesla), the lower of which coincides with the observed peak. The rf$\|$dc peak at 0.21 Tesla is close to the acoustic mode predicted at 0.19 Tesla. The peaks at fields lower than 0.1 Tesla are not predicted and could be attributed to domain effects which go beyond our micromagnetic model. In short, we claim that since the preferential excitation of either acoustic or optical modes depends on the orientation of the exciting field with respect to the magnetization direction, the variation of the magnetization profile along the multilayer thickness favours the emergence of mixed modes that can qualitatively explain the data. In contrast, if we simulate a simple SAF bilayer, which does not allow for any variation of the magnetization along its thickness, this mechanism of mixed mode creation ceases to work (Fig. 7).

Conclusions

We have studied Ferromagnetic Resonance (FMR) in two series of $[Ru_{10}/Co_x]_{12}$ and $[Ru_6/Cr_3/Co_x)]_{12}$, x = 16–60 Å, SAF-multilayers prepared by sputter deposition having easy-plane anisotropy and zero anisotropy within the plane.

The resonance fields of the acoustic modes are in good agreement with the values predicted by macrospin models when using the interlayer exchange and anisotropy fields independently derived by the quasistatic (VSM) magnetic measurements. The optical modes are more interesting as they can give high frequencies at zero-applied field. However, to observe optical modes by cavity FMR, $\gamma\sqrt{2H_{ex}H_K}$ must exceed the resonance frequency of the cavity. For the $[Ru_6/Cr_3/Co_x)]_{12}$ series the values of anisotropy and exchange fields were low and the optical modes were not accessible. For the $[Ru_{10}/Co_x]_{12}$ series the resonance fields of the optical modes are lower than expected. We attribute this to the existence of hybridized mixed modes as the resonances for these samples appear within the region where the optical modes are split. Although the micromagnetic simulations in Fig. 5 indicate that the hybridized modes can be observed for both rf$\perp$dc and rf$\|$dc we have experimentally observed only the latter. This may be attributed to the FMR signals for the acoustic modes being one order of magnitude greater. The existence of inhomogeneous modes that can be described as coupled acoustic and optical modes has been previously reported[20,23] and gained renewed interest lately.[4,5,19] The coupling mechanism is related to asymmetry due to obliquely applied external magnetic fields or of the sample itself. Since the preferential excitation of either acoustic or optical modes depends on the orientation of the exciting field with respect to the magnetization direction, the variation of the magnetization profile along the multilayer thickness, revealed by our micromagnetic simulations, implies the emergence of such hybridized modes. Thus, mode mixing is not limited to near the region where the frequencies of the optical and acoustic modes coincide.

Conflicts of interest

There are no conflicts to declare.

Acknowledgements

The research work was supported by the Hellenic Foundation for Research and Innovation (HFRI) under the 3rd Call for HFRI PhD Fellowships (Fellowship Number: 5383).

References

1 D. E. Bürgler, in: *Handbook of Magnetic Materials*, ed., K. H. J. Buschow, 2001, **13**.
2 A. Fert, *Rev. Mod. Phys.*, 2008, **80**, 1517–1530.
3 M. Ishibashi, Y. Shiota, T. Li, S. Funada, T. Moriyama and T. Ono, *Sci. Adv.*, 2020, **6**, eaaz6931.
4 A. Sud, C. W. Zollitsch, A. Kamimaki, T. Dion, S. Khan, S. Iihama, S. Mizukami and H. Kurebayashi, *Phys. Rev. B*, 2020, **102**, 100403.
5 Y. Shiota, T. Taniguchi, M. Ishibashi, T. Moriyama and T. Ono, *Phys. Rev. Lett.*, 2020, **125**, 17203.
6 T. Seki, H. Tomita, A. A. Tulapurkar, M. Shiraishi and T. Shinjo, *Appl. Phys. Lett.*, 2009, **94**, 212505.
7 B. Jianga, W. Zhanga, H. Zhonga, Y. Zhanga, S. Yua, G. Hana, S. Xiaoa, G. Liua, S. Yana, J. Lib and S. Kang, *J. Magn. Magn. Mater.*, 2019, **490**, 165470.
8 R. Cheng, D. Xiao and A. Brataas, *Phys. Rev. Lett.*, 2016, **116**, 207603.
9 P. Grünberg, R. Schreiber, Y. Pang, U. Walz, M. B. Brodsky and H. Sowers, *J. Appl. Phys.*, 1987, **61**, 3750–3752.
10 R. A. Duine, K. J. Lee, S. S.-P. Parkin and M. D. Stiles, *Nat. Phys.*, 2018, **14**, 217–219.
11 H. J. Waring, N. A.-B. Johansson, I. J. Vera-Marun and T. Thomson, *Phys. Rev. Appl.*, 2020, **13**, 034035.
12 Y. Gong, Z. Cevher, M. Ebrahim, J. Lou, C. Pettiford, N. X. Sun and Y. H. Ren, *J. Appl. Phys.*, 2009, **106**, 063916.
13 X. Xing, M. Liu, S. Li, O. Obi, J. Lou, Z. Zhou, B. Chen and N. X. Sun, *IEEE Trans. Magn.*, 2011, **47**, 3104–3107.
14 R. B. Morgunov, A. V. Yurov, V. A. Yurov, A. D. Talantsev, A. I. Bezverhnii and O. V. Koplak, *Phys. Rev. B*, 2019, **100**, 144407.
15 S. Li, Q. Li, J. Xu, S. Yan, G. X. Miao, S. Kang, Y. Dai, J. Jiao and Y. Lü, *Adv. Funct. Mater.*, 2016, **26**, 3738–3744.
16 S. Li, C. Wang, X. M. Chu, G. X. Miao, Q. Xue, W. Zou, M. Liu, J. Xu, Q. Li, Y. Dai, S. Yan, S. Kang, Y. Long and Y. Lü, *Sci. Rep.*, 2016, **6**, 33349.
17 A. Kamimaki, S. Iihama, T. Taniguchi and S. Mizukami, *Appl. Phys. Lett.*, 2019, **115**, 132402.
18 P. Grünberg, R. Schreiber, Y. Pang, M. B. Brodsky and H. Sowers, *Phys. Rev. Lett.*, 1986, **57**, 2442.
19 C. Dai and F. Ma, *Appl. Phys. Lett.*, 2021, **118**, 112405.
20 Z. Zhang, L. Zhou, P. E. Wigen and K. Ounadjela, *Phys. Rev. B: Condens. Matter Mater. Phys.*, 1994, **50**, 6094.
21 H. Zabel, *Philos. Mag. B*, 2000, **80**, 293–306.
22 See for instance §3.1 in D. E. Bürgler, P. Grünberg, S. O. Demokritov and M. T. Johnson, *Handb. Magn. Mater.*, 2001, **13**, 1–85.
23 N. M. Kreines, D. I. Kholin, V. F. Meshcheryakov, M. A. Milyaev, L. N. Romanshev and V. V. Ustinov, *JETP Lett.*, 1998, **67**(9), 727–732.
24 I. Benguettat-El Mokhtari, A. Mourkas, P. Ntetsika, I. Panagiotopoulos, Y. Roussigné, S. M. Cherif, A. Stashkevich, F. Kail, L. Chahed and M. Belmeguenai, *J. Appl. Phys.*, 2019, **126**, 133902.
25 A. Vansteenkiste, J. Leliaert, M. Dvornik, M. Helsen, F. Garcia-Sanchez and B. V. Waeyenberge, *AIP Adv.*, 2014, **4**, 107133.
26 X. Liu, M. M. Steiner, R. Sooryakumar, G. A. Prinz, R. F.-C. Farrow and G. Harp, *Phys. Rev. B: Condens. Matter Mater. Phys.*, 1996, **53**, 12166.
27 D. Kumar and A. O. Adeyeye, *J. Appl. Phys.*, 2017, **50**, 343001.